Ocean Dynamics (2017) 67:1335–1350
DOI 10.1007/s10236-017-1088-6

On the modifications of near-inertial waves at fronts: implications for energy transfer across scales

Leif N. Thomas[1]

Received: 30 October 2016 / Accepted: 10 July 2017 / Published online: 4 August 2017

Abstract In the ocean, wind-generated kinetic energy (KE) manifests itself primarily in balanced currents and near-inertial waves. The dynamics of these flows is strongly constrained by the Earth's rotation, causing the KE in balanced currents to follow an inverse cascade but also preventing wave-wave interactions from fluxing energy in the near-inertial band to lower frequencies and higher vertical wavenumbers. How wind-generated KE is transferred to small-scale turbulence and dissipated is thus a non-trivial problem. This article presents a review of recent theoretical calculations and numerical simulations that demonstrate how some surprising modifications to internal wave physics by the lateral density gradients present at ocean fronts allow for strong interactions between balanced currents and near-inertial waves that ultimately result in energy loss for both types of motion.

Keywords Fronts · Internal waves · Wave-mean flow interactions

This article is part of the Topical Collection on the *48th International Liège Colloquium on Ocean Dynamics, Liège, Belgium, 23–27 May 2016*

Responsible Editor: Amala Mahadevan

✉ Leif N. Thomas
leift@stanford.edu

[1] Department of Earth System Science, Stanford University, Stanford, CA, USA

1 Introduction

Winds blowing over the ocean generate currents with a range of frequencies. The bulk of the kinetic energy (KE) in these flows is contained in mesoscale currents and eddies with low frequencies, which are strongly constrained by the Earth's rotation to follow the geostrophic balance. Winds also generate near-inertial waves (NIWs), which are oscillatory, unbalanced motions with frequencies close to the inertial frequency $f = 2\Omega \sin\phi$ (Ω is the Earth's angular velocity and ϕ latitude). The dissimilar temporal scales of the balanced, mesoscale currents, and the NIWs suggest that the two types of motion should not interact very effectively, and that the fast waves should simply pass through the balanced flows without exchanging energy or momentum. While this is a fairly accurate characterization for weak currents, this does not hold for energetic flows, such as those found in western boundary currents and the Antarctic Circumpolar Current. These regions also coincide with the maxima in NIW kinetic energy (e.g., Elipot et al. 2010), suggesting that strong interactions between NIWs and balanced motions should be prevalent at these locations. Such interactions have been hypothesized to play an important role in the kinetic energy budgets for both types of motions through damping the balanced circulation and facilitating a transfer of KE from NIWs to higher frequency internal waves and potentially to small-scale turbulence (Ferrari and Wunsch 2009; Polzin 2010; Polzin and Lvov 2011; Nagai et al. 2015). Recent idealized, high-resolution simulations of wind-forced flows support this hypothesis and suggest that, integrated globally, the rate of KE extracted from the balanced circulation by NIWs could be of order 0.1 TW (Taylor and Straub 2016; Barkan et al. 2017).

Not surprisingly, the hotbeds of NIW-balanced flow interactions are ocean fronts, where strong vertical vorticity and horizontal density gradients conspire to significantly modify the physics of the waves. The vertical vorticity of geostrophic currents, ζ_g, shifts the net spin of the fluid away from $f/2$, causing inertial motions to oscillate at the effective inertial frequency $f_{eff} = \sqrt{f(f+\zeta_g)}$ (Healey and LeBlond 1969; Mooers 1975; Olbers 1981; Kunze 1985).[1] Lateral variations in ζ_g and f_{eff} further modify the horizontal wavenumber of NIWs and enhance their vertical propagation (van Meurs 1998; Young and Ben-Jelloul 1997; Balmforth and Young 1999). In so doing, the waves acquire potential energy at the expense of the energy in the balanced flow (Xie and Vanneste 2015). NIW-mean flow interactions associated with vertical vorticity can also trigger wave-wave interactions that transfer KE from the inertial peak to higher frequencies (e.g., Wagner and Young 2016).

The intense lateral density gradients characteristic of ocean fronts modify the physics of NIWs in ways that are less intuitive than the vertical vorticity described above, causing NIWs to exhibit rather unexpected behavior. For example, NIW velocity hodographs do not trace inertial circles but are instead elliptical, the vertical components of the group and phase velocity can be in the same direction, and the direction of energy propagation is symmetric about the slope of isopycnals not the horizontal. This atypical wave physics can facilitate energy transfers between NIWs, inertia-gravity waves of different frequencies, and balanced currents. The objective of this article is to review recent work that describes this physics and discusses the implications for the energetics of both the near-inertial wave field and balanced circulation in the ocean. The focus is on NIWs that are presumed to have been generated externally by winds as opposed to internally by frontal processes, since the energy exchange with the mean flow that transpires in either case is different in nature. Therefore, the literature on geostrophic adjustment (e.g., Zeitlin et al. 2003; Shakespeare and Taylor 2013) and spontaneous imbalance and emission of inertia-gravity waves at fronts (e.g. Vanneste 2013; Shakespeare and Taylor 2014; Nagai et al. 2015; Shakespeare and Hogg 2017) will not be reviewed here.

2 Modifications of near-inertial wave properties at fronts

The key to comprehending how fronts facilitate wave-mean flow interactions is to understand how lateral density gradients modify the propagation, frequency, and polarization relations of NIWs. For the latter two properties, the most insightful way to do this is to use parcel arguments and the principles of conservation of buoyancy and absolute momentum that govern the basic physics of inertia-gravity waves (e.g., Holton 2004, Section 7.5).

2.1 Parcel arguments and the minimum frequency of inertia-gravity waves

Buoyancy, $b = -g\rho/\rho_o$, (g is the acceleration due to gravity, ρ is the density, and ρ_o a reference density) is conserved when diabatic processes (caused by heating, cooling, or mixing of heat and salt, for example) are absent. Absolute momentum is an angular momentum-like quantity that is conserved in currents that are inviscid and that do not have spatial variations in the direction of their flow (which is a fairly good approximation at fronts). Take for example a current in the x-direction that satisfies these assumptions. In this limit, both friction and pressure gradient forces in the along flow direction are zero, and the momentum equation in the x-direction can be written as

$$\frac{DM}{Dt} = 0 \tag{1}$$

where $M = u - fY$ is the absolute momentum, Y is the displacement of fluid parcels in the y-direction, and D/Dt is the material derivative. Thus $\Delta M \equiv \int (DM/Dt)dt = 0$, where Δ is the change following fluid parcels. Splitting the flow into two components, $u = u_g + u'$, one associated with the front, u_g, and the other with the wave, u', conservation of absolute momentum implies that

$$u' = -\Delta M_g \tag{2}$$

where $M_g \equiv u_g - fY$ is the absolute momentum of the background flow and $u' = 0$ at $t = 0$. The buoyancy can be decomposed in a similar fashion, $b = b_g + b'$, and if it is conserved the wave buoyancy anomaly is

$$b' = -\Delta b_g, \tag{3}$$

where it is assumed $b' = 0$ at $t = 0$. Wave buoyancy and velocity anomalies drive forces, the latter associated with the Coriolis force $-fu'$, that when restoring explain the oscillatory behavior of inertia-gravity waves.

For instance, in the textbook example with no background flow ($u_g = 0$) and a density field with flat isopycnals and stratification $N^2 = \partial b_g/\partial z$, small-amplitude vertical displacements, Z, generate a buoyancy anomaly and hence vertical acceleration $D^2Z/Dt^2 = b' = -N^2Z$, yielding oscillations at a frequency $\omega = N$. In this case, isosurfaces of the absolute momentum of the background flow, known as M-surfaces, are vertical (Fig. 1, upper left panel). Consequently, fluid parcel displacements in the y-direction cross M-surfaces and generate a velocity anomaly, Coriolis

[1] This expression for f_{eff} is only valid for straight fronts. If the front is curved, inertial motions oscillate at a frequency that depends on the flow curvature as well, see for example Kunze and Boss (1998).

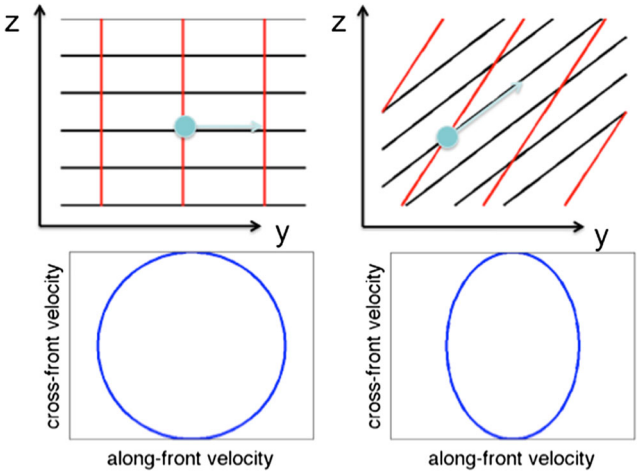

Fig. 1 *Upper panels*: isopycnals (*black*) and $M-$surfaces (*red*) for no background flow (*left*) and at a front (*right*), where thermal wind shear and horizontal density gradients tilt the two surfaces toward one another and reduce the along-isopycnal gradient in absolute momentum. Consequently, at fronts along-isopycnal displacements of fluid parcels (*blue arrows*), which lead to inertia-gravity waves with the minimum frequency, result in a reduced along-front wave velocity, u', Coriolis force, and frequency. In addition, hodographs of the wave velocity (*bottom panels*) shift from inertial circles when there is no background flow (*left*) to ellipses with stronger flow in the cross-front direction at a front (*right*)

force, and lateral acceleration $D^2Y/Dt^2 = -fu' = -f^2Y$ but no buoyancy anomaly, and hence result in oscillations at a frequency $\omega = f$. For most oceanic conditions, $N > f$, and consequently inertia-gravity waves in the absence of a background flow span a range of frequencies between f and N as fluid parcel displacements move from being purely horizontal to purely vertical.

Fronts distort the geometry of isopycnals and M-surfaces, leading to profound modifications to the properties inertia-gravity waves. The baroclinicity of the front, which can be quantified with the thermal wind relation

$$S^2 \equiv -\frac{\partial b_g}{\partial y} = f\frac{\partial u_g}{\partial z}, \tag{4}$$

tilts both isopycnals and M-surfaces (Fig. 1, upper right panel).[2] As the baroclinicity increases (keeping all other properties of the background flow constant), M-surfaces flatten while isopycnals steepen and the two surfaces angle toward one another. In this system, the inertia-gravity waves with the lowest frequency correspond to parcel displacements that are along-isopycnal (since they do not induce a buoyancy force), and result in oscillations caused by the Coriolis force, similar to the case without a background flow. However, the change in absolute momentum that the fluid parcels experience at a front, and hence the Coriolis force, is reduced because the along-isopycnal gradient in M is weakend by baroclinicity. The expression for the minimum frequency of inertia-gravity waves in a background flow reflects this physics

$$\omega_{min} = \sqrt{-f\nabla_\rho M_g} = f\sqrt{1 + Ro_g - 1/Ri_g}, \tag{5}$$

where $\nabla_\rho M$ is the along-isopycnal gradient in absolute momentum, which can also be written in terms of the gradient Rossby number

$$Ro_g = \frac{\zeta_g}{f} = \left(-\frac{\partial u_g}{\partial y}\right)\Big/ f \tag{6}$$

(which unlike the bulk Rossby number can be positive or negative depending on the sign of the vertical vorticity) and Richardson number of the geostrophic flow

$$Ri_g = \frac{N^2}{(\partial u_g/\partial z)^2} = \frac{N^2 f^2}{S^4} \tag{7}$$

(for a derivation of this expression see Whitt and Thomas 2013). The main message to take from (5) is that baroclinicity permits wave frequencies that are less than the effective inertial frequency $f_{eff} = f\sqrt{1 + Ro_g}$. In particular, for sufficiently low Richardson numbers, namely $Ri_g \to 1/(1 + Ro_g)$, $\omega_{min} \to 0$ and the distinction in time scales between the waves and balanced currents is lost.

2.2 Polarization relations at the minimum frequency

For inertia-gravity waves at the minimum frequency, the polarization relation between the magnitudes of three components of the wave velocity is

$$\left(|u'_{min}|, |v'_{min}|, |w'_{min}|\right) = |v'_{min}|\left(\frac{\omega_{min}}{f}, 1, |s_\rho|\right), \tag{8}$$

where $s_\rho = S^2/N^2$ is the slope of isopycnals (Whitt and Thomas 2013). Thus velocity hodographs of waves of minimum frequency do not trace perfect inertial circles but are instead ellipses with a major axis pointed in the cross-front direction (i.e. $|u'_{min}| < |v'_{min}|$) when $\omega_{min} < f$ (Fig. 1, lower panels). This follows from conservation of absolute momentum and the reduction of $|\nabla_\rho M|$ by baroclinicity. In addition, the hodographs are aligned with isopycnals which are tilted in the vertical, imparting a vertical velocity to the waves. These modifications can allow the waves to flux momentum in the vertical and make the wave momentum fluxes anisotropic in the horizontal. This has important implications for the energetics of NIWs, as will be highlighted in Sections 3 and 5.

2.3 Dispersion relation and wave propagation

While parcel arguments are useful for understanding the restoring forces for NIWs in fronts, they cannot be used to characterize wave propagation. Instead, a WKB-type

[2]Note that since the front is two-dimensional, there is no geostrophic flow nor thermal wind shear in the y-direction.

analysis of the governing wave equation is the most straightforward approach to derive the waves' dispersion relation and group velocity.

Two-dimensional NIW are governed by the time-dependent, hydrostatic Eliassen-Sawyer equation

$$\left(\frac{\partial^2}{\partial t^2}+f_{eff}^2\right)\frac{\partial^2\psi'}{\partial z^2}+2S^2\frac{\partial^2\psi'}{\partial y\partial z}+N^2\frac{\partial^2\psi'}{\partial y^2}=0, \tag{9}$$

where the wave velocity is related to the streamfunction in the usual way $v'=\partial\psi'/\partial z$, $w'=-\partial\psi'/\partial y$ (Sawyer 1956; Eliassen 1962; Whitt and Thomas 2013). Assuming slow spatial variations in the background flow, plane wave solutions of the form $\psi'\sim\exp[i(ly+mz-\omega t)]$ with wavevector (l,m) and frequency ω can be sought, yielding the dispersion relation

$$\omega^2=f_{eff}^2+2S^2\gamma+N^2\gamma^2, \tag{10}$$

where $\gamma=l/m$. Similar relations were first derived by Mooers (1975) in the non-hydrostatic limit and by Kunze (1985) for fronts with weak vorticity and baroclinicity (i.e., with $Ro_g\ll 1$ and $Ri_g\gg 1$). The group velocity can be calculated from Eq. 10 as

$$\mathbf{c}_g\equiv\left(\frac{\partial\omega}{\partial l},\frac{\partial\omega}{\partial m}\right)=\left(\frac{S^2+N^2\gamma}{\omega m}\right)(1,-\gamma)\,. \tag{11}$$

It follows that the direction of energy propagation with respect to the horizontal, that is, the slope of wave characteristics, is

$$\frac{c_{g,z}}{c_{g,y}}=-\gamma=s_\rho\mp\sqrt{\frac{\omega^2-\omega_{min}^2}{N^2}}. \tag{12}$$

For waves of a given frequency (excluding the minimum frequency), there are four possible directions of energy propagation, similar to inertia-gravity waves in the absence of a background flow. However, unlike the no-flow case, at a front the directions of propagation are symmetric about isopycnals not the horizontal (Fig. 2). Consequently, for waves at the effective inertial frequency, $\omega=f_{eff}$, two characteristics slopes are possible $\gamma=0$ and $-\gamma=2s_\rho$, in contrast to the case of no front where only the $\gamma=0$ characteristic and horizontal propagation is allowed. This leads to unusual rules for wave reflection off boundaries that can make NIWs undergo critical reflections during which energy from both the waves and mean flow is dissipated, as will be discussed in Section 4.

2.4 Summary of modifications

Horizontal density gradients at fronts modify the properties of NIWs in three important ways: first, by reducing the minimum frequency of inertia-gravity waves (5) they support waves with frequencies less than the effective inertial frequency f_{eff}; second, by adjusting the direction of energy propagation (12) they allow waves at the effective inertial frequency to transmit energy vertically as well as horizontally; and third, fronts permit vertical and anisotropic horizontal wave momentum fluxes as a consequence of the polarization relation (8). These modifications are important because they are responsible for phenomena that could help close the energy budgets of both the NIW field and balanced circulation, as will be described in the next three sections.

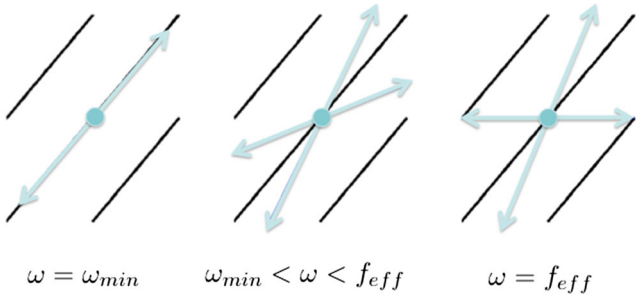

Fig. 2 The directions of energy propagation for NIWs, i.e., the ray paths, (*blue arrows*) are parallel to isopycnals (*black lines*) at the minimum frequency ω_{min} (*left*) and progressively move away from the isopycnal slope as the frequency is increased. This is very different from NIWs in the absence of background currents, which propagate horizontally at the minimum frequency. At a front, horizontal propagation only occurs for waves at the effective inertial frequency, $\omega=f_{eff}$, yet these waves can also propagate vertically on a steep characteristic with twice the isopycnal slope

3 Parameteric subharmonic instability at fronts

In the upper ocean, the majority of the kinetic energy (KE) in the internal wave spectrum is found near the inertial frequency (Ferrari and Wunsch 2009). How NIWs lose their KE is not well understood although shear instabilities and wave absorption at critical layers have been proposed as possible damping mechanisms (Alford and Gregg 2001; Kunze et al. 1995). Wave-wave interactions, in contrast, are thought to transfer energy to low frequencies and hence increase rather than reduce the energy in the inertial peak (McComas and Bretherton 1977; Müller et al. 1986). One wave-wave interaction, parametric subharmonic instability (PSI), is characterized by a transfer of energy from a wave of a given frequency to its subharmonic at half its frequency. Since NIWs have the lowest frequencies of all inertia-gravity waves according to classical internal wave theory, they cannot lose energy via PSI. However, this reasoning no longer holds at fronts because baroclinicity permits inertia-gravity waves with subinertial frequencies, e.g., Eq. 5. Indeed, Thomas and Taylor (2014) demonstrated using a stability analysis and numerical simulations that inertial waves in fronts can be damped by PSI under certain conditions. The key findings from this work are summarized in this section.

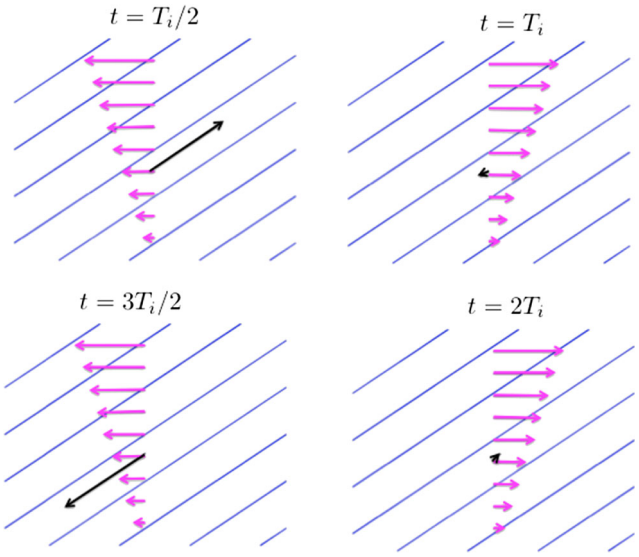

Fig. 3 Schematic of the basic state of the stability analysis used to study a parametric subharmonic instability that extracts kinetic energy from inertial motions at fronts. A vertically-sheared inertial oscillation (velocity vectors in *magenta*) at a front (isopcynals in *blue*) is perturbed by a flow that is purely isopycnal (velocity vector in *black*). Four snapshots are shown, at $1/2, 1, 3/2$, and 2 inertial periods, T_i, and for a front with $Ri_g = 4/3$

Thomas and Taylor (2014) considered a vertically-sheared inertial oscillation superimposed on a simple front with uniform gradients (Fig. 3). The frontal flow had no vertical vorticity and hence the inertial motion oscillated at a frequency $f_{eff} = f$. Therefore, the condition for PSI to develop at the front is $\omega_{min} \leq f/2$, which using (5) translates to a critical Richardson number of $Ri_g = 4/3$. Thomas and Taylor (2014) tested this prediction using a stability analysis in which the basic state was perturbed with a two-dimensional (invariant in the along-front direction) plane wave corresponding to an inertia-gravity wave of minimum frequency, i.e. with flow that is aligned with isopcynals (Fig. 3, black arrows). Time series of the cross-front velocity of the perturbations for three values of the Richardson number $Ri_g = 7/6, 4/3$, and $3/2$ illustrate the expected increase in frequency of the perturbation, but also growth for $Ri_g = 4/3$ when $\omega_{min} = f/2$ and PSI is active (Fig. 4, middle panel). This result is for weak inertial shear. The stability analysis revealed that the instability criterion is also a function of the strength of the inertial shear relative to the thermal wind shear. When it is weak, PSI occurs near $Ri_g = 4/3$ as illustrated above, but as the two shears become comparable, PSI can develop for a range of values of Ri_g centered about $4/3$ since the inertial shear affects the properties of the waves (Thomas and Taylor 2014).

PSI gains energy by extracting KE from the inertial oscillation at a rate given by the ageostrophic shear production

$$AGSP = -v'w'\frac{\partial \overline{v}}{\partial z} \tag{13}$$

where $\overline{v}$ is the cross-front velocity of the inertial motion and v', w' are the velocity components of the perturbation. Since the perturbation is a wave of minimum frequency, its velocity is along-isopycnal and v' and w' are correlated following the polarization relation (8). This results in a vertical wave momentum flux that can lead to a net extraction of KE from the inertial oscillation with $AGSP > 0$ when the flux is phased correctly with the inertial shear (Fig. 4, bottom panel). This phasing is achieved when $\omega_{min} = f/2$ (namely

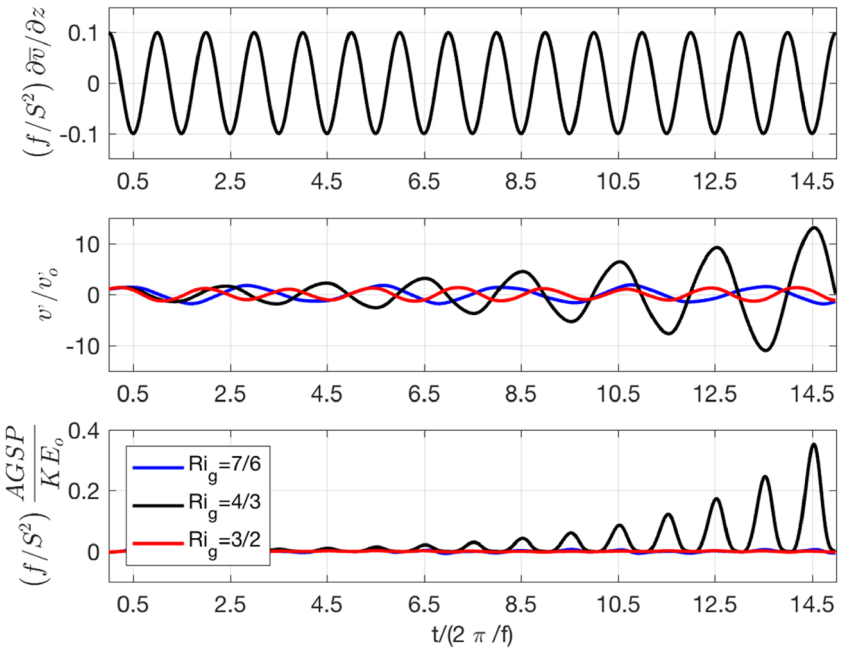

Fig. 4 Results from the stability analysis for a basic state similar to that shown in Fig. 3, but with three different Richardson numbers of the frontal flow $Ri_g = 7/6, 4/3, 3/2$ (*blue, black, and red lines*, respectively) yet the same inertial shear (*top panel*, normalized by the thermal wind shear S^2/f). Time series of the perturbation cross-front velocity (*middle panel*, normalized by its initial value) and the ageostrophic shear production (13) (*bottom panel*, normalized by $(S^2/f)KE_o$, where KE_o is the initial kinetic energy of the perturbation). Time is expressed in units of inertial periods

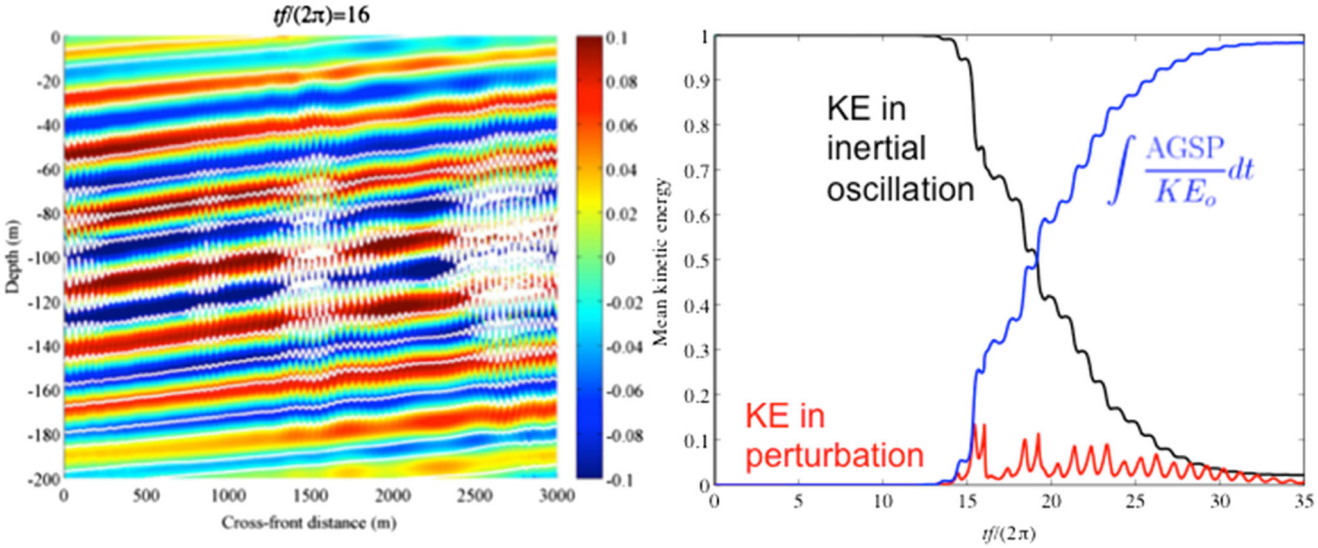

Fig. 5 *Left*: The cross-front velocity (color shading, in units of m s^{-1}) and isopycnals (*white contours*) at 16 inertial periods into a numerical simulation of a front with inertial shear, similar to the set up shown in Fig. 3, however initialized with perturbations taking the form of random noise. Over time perturbations with flow parallel to isopycnals grow out of the noise and develop Kelvin-Helmholtz billows that are evident in the fine-scale structures in density. *Right*: Time series from the simulation of the kinetic energy in the inertial shear (*black*) and the perturbations (*red*), and the kinetic energy removed from the inertial shear by the perturbations $\int AGSPdt$. Variables are normalized by the initial kinetic energy in the inertial oscillation and time by an inertial period

when the perturbation wave is a subharmonic of the inertial motion, hence the PSI) and when the times of minimum inertial shear and maximum $|v'|$ coincide (c.f. Fig. 4, top and middle panels, black lines).[3]

Thus, at fronts, PSI can remove KE from inertial motions, but what is the ultimate fate of this energy? Nonlinear, non-hydrostatic, high-resolution numerical simulations were used by Thomas and Taylor (2014) to address this question and test the stability analysis. The simulations were configured with a front and inertial oscillation similar to that used in the stability analysis; however, the perturbations were initialized with random noise rather than a plane wave. Out of the noise, an unstable mode with flow parallel to isopycnals grows under the conditions for PSI to develop predicted by the stability analysis (Fig. 5, left panel). As it grows in amplitude, the unstable mode develops secondary shear instabilities, creating Kelvin-Helmholtz billows in the regions of strong shear where the Richardson number of the total flow drops below a quarter. The unstable mode extracts KE from the inertial shear via the AGSP, consistent with the stability analysis. However, the amount of KE contained in the perturbations saturates at a value much less than the total KE removed from the inertial motion (Fig. 5, right panel). The remaining KE is not stored in the unstable mode, but is instead either lost through viscous dissipation or increases the potential energy of the system through mixing density by the small-scale shear instabilities. It is important to realize that these shear instabilities would not form in the absence of the PSI because the minimum Richardson number of the combined geostrophic and inertial motions is above the criterion for Kelvin-Helmholtz instability. By enhancing the vertical shear, the growth of the PSI lowers the Richardson number to subcritical values, thereby opening a pathway to turbulence where KE in inertial motions is transferred to small scales and lost.

[3]This is true for a front with upward sloping isopycnals where v' and w' are positively correlated as shown in Fig. 3, and as used in the stability analysis plotted in Fig. 4. When isopycnals slope downward, the times of *maximum* inertial shear and maximum $|v'|$ must coincide for PSI to develop since v' and w' are anti-correlated in that case.

4 Critical reflection of near-inertial waves at fronts

Apart from wave-wave interactions such as PSI, inertia-gravity waves can lose energy during reflections off boundaries. This is especially true if they experience critical reflection, when the direction of energy propagation of the reflected wave runs parallel to the boundary (Ivey and Nokes 1989). According to classical internal wave theory ($u_g = 0$), inertial waves with $\omega = f_{eff} \equiv f$ cannot experience critical reflection because they only propagate horizontally. At fronts, however, this conclusion does not hold because inertial waves can propagate in the vertical as well as in the horizontal (e.g. Fig. 2). Using analytical theory and numerical simulations, Grisouard and Thomas

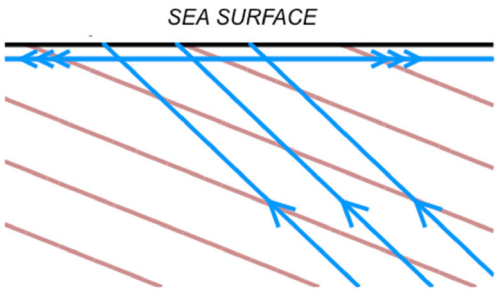

Fig. 6 At a front (isopycnals in *brown*), a beam of energy associated with a vertically propagating inertial wave with $\omega = f_{eff}$ (*blue*, *upward sloping lines*), will be compressed into an infinitesimally-thin area when the wave reflects off the sea surface. Under these conditions the wave experiences critical reflection and amplifies

(2015) and Grisouard and Thomas (2016) demonstrated that inertial waves can indeed experience critical reflection as a consequence of this physics. A summary of this work is presented in this section.

If an inertial wave is propagating vertically in a front along the tilted ray path shown in the righthand panel of Fig. 2, when it hits a boundary it must reflect along the horizontal characteristic with $\gamma = 0$. Consequently, if the boundary is flat, a beam of inertial wave energy will be compressed into an infinitesimally thin area upon reflection and the wave must amplify to conserve its energy. This is the condition for critical reflection and it can occur at fronts off the nominally-flat sea surface (Fig. 6). Grisouard and Thomas (2015) tested this idea using linear and nonlinear two-dimensional (i.e., invariant in the x-direction) numerical simulations. The simulations were forced by a wave maker at depth that was designed to generate upward propagating inertial waves on the steep characteristic of Eq. 12 and the background front had no vertical vorticity

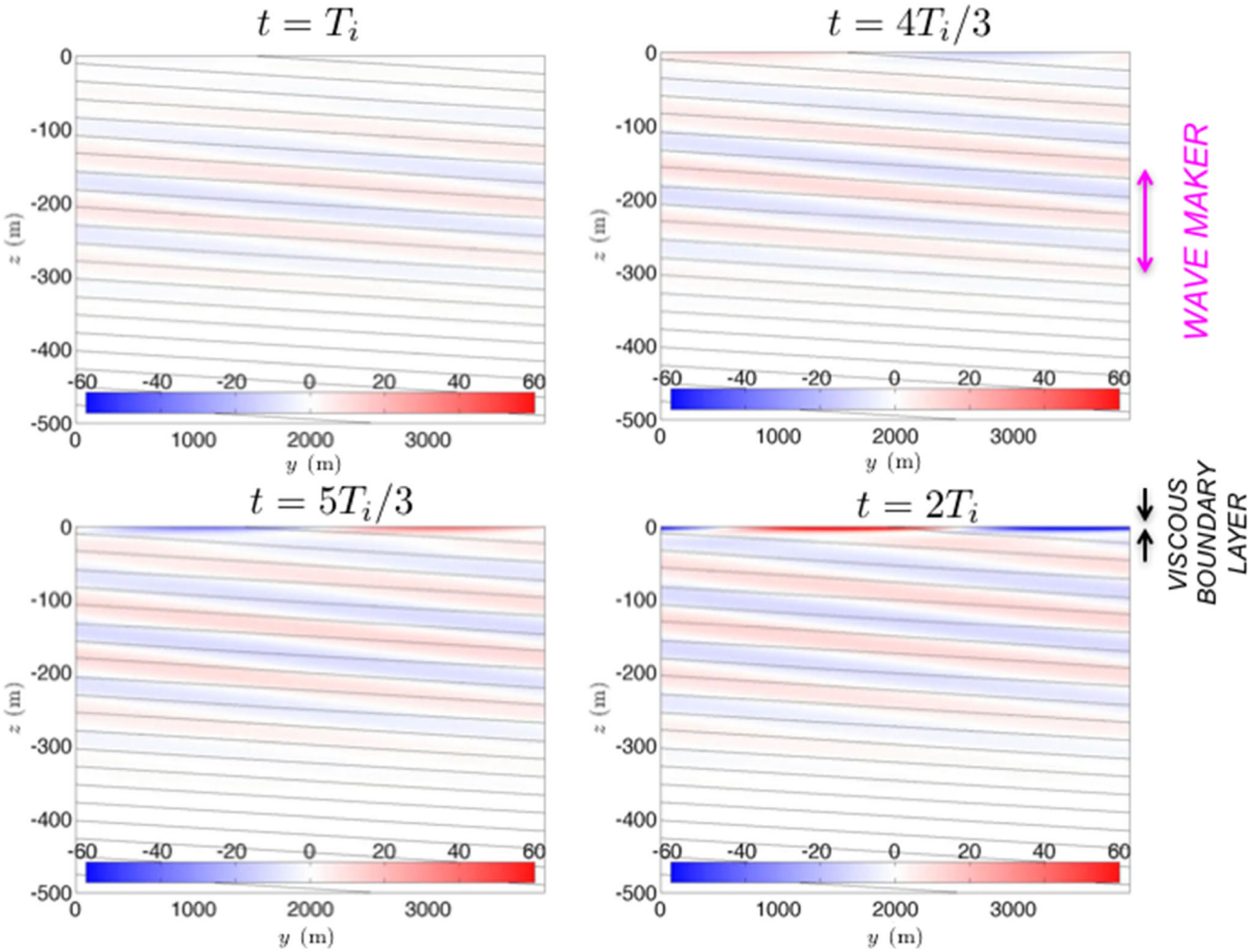

Fig. 7 Snapshots of the along-front component of the vorticity (normalized by f) of an inertial wave (i.e., with frequency $\omega = f$) at $1, 4/3, 5/3$, and 2 inertial periods in a front with isopycnals in *black* from a linear numerical simulation. Note that the flow is invariant in the along-front x-direction and the cross-front coordinate is y. The wave is forced by a wave maker at the depth indicated by the *magenta arrow* to the right that generates an upward propagating inertial wave packet. As the waves hit the surface, they experience a critical reflection and generate a thin viscous boundary layer

such that $f_{eff} = f$. In the linear simulations, inertial waves on the steep characteristic are amplified upon reflection, but the amplification is limited by friction in a thin viscous boundary layer that develops near the surface (Fig. 7). In the nonlinear simulations, bores and higher harmonics form via wave-wave interactions, resulting in a thicker layer over which the effects of critical reflection are felt (Grisouard and Thomas 2015), but the basic energetics of the phenomenon are qualitatively similar.

The energy fluxed upward by the wave maker,

$$\text{Incoming Flux} = \frac{1}{\rho_o}\int p'w'dy, \tag{14}$$

(where p' is the wave pressure perturbation, and the integral is made over the width of the domain) is dissipated in the boundary layer during critical reflection. However, the total dissipation of wave energy (both kinetic and potential),

$$\text{Dissipation} = \nu\int\int\left(\mathbf{u}'\cdot\frac{\partial^2\mathbf{u}'}{\partial z^2} + \frac{b'}{N^2}\frac{\partial^2 b'}{\partial z^2}\right)dydz, \tag{15}$$

(where ν is the constant viscosity and diffusivity used in the simulations and the integral is made over a control volume that spans the width and upper 15 m of the domain) exceeds the incoming flux for waves near critical reflection with $\omega \approx f$ (Fig. 8, upper panel) (Grisouard and Thomas 2016). Clearly, there must be an additional source of wave energy besides the wave maker to explain this excess dissipation. This extra energy originates from the front and is liberated by the waves at a rate

$$\text{Energy exchange with Front} = \int\int\left(-u'w'\frac{S^2}{f} + v'b'\frac{S^2}{N^2}\right)dydz, \tag{16}$$

where the control volume is the same as that used in Eq. 15 (Fig. 8, bottom panel). Near critical reflection, the waves preferentially remove the front's potential energy over its kinetic energy via the second term in Eq. 16, indicating that they act to mix the frontal lateral density gradient.

The rate of energy removed from the front depends on both the wave frequency and the strength of the fronts, as measured by the Richardson number (Fig. 8, bottom panel). The energy exchange with the front involves correlations between the wave velocity components and its buoyancy anomaly. Friction enhances these correlations, consequently they are largest at near-inertial frequencies where viscous effects are most prominent due to the compression of the waves' vertical scale near critical reflection (Grisouard and Thomas 2016). The peak energy exchange at near-inertial frequencies decreases with increasing Richardson number, which is to be expected since the front is weaker. In addition,

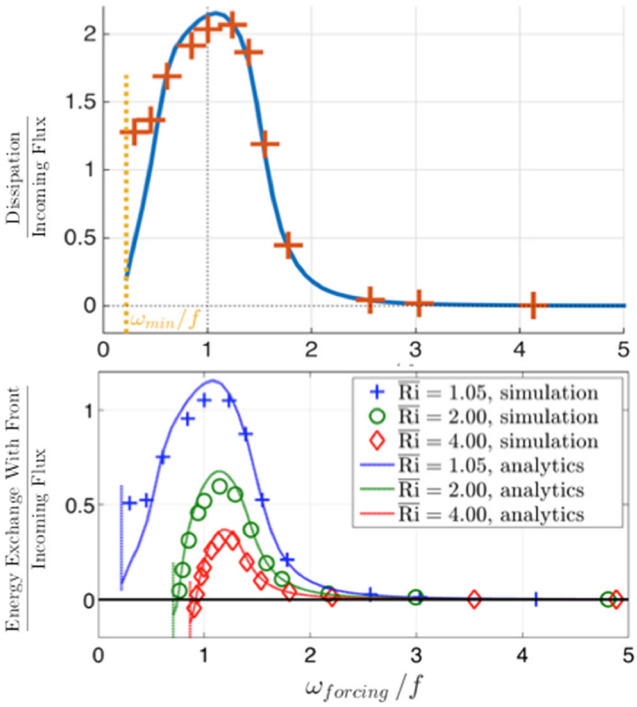

Fig. 8 *Top panel*: the dissipation of energy integrated over a control volume that spans the upper 15 m of the domain, (15), normalized by the energy flux of the upward propagating wave, (14), as a function of the forcing frequency of the wave generator, $\omega_{forcing}$. The Richardson number of the front is $Ri_g = 1.05$, with a minimum wave frequency indicated by the vertical, *yellow dashed line*. *Bottom panel*: the rate of energy exchange with the front integrated over a control volume that spans the upper 15 m of the domain, (16), normalized by the energy flux of the upward propagating wave, (14), as a function of the forcing frequency of the wave generator, for three different frontal flows with Richardson numbers $Ri_g = 1.05$, 2, and 4. *Solid lines* (markers) indicate results from the theory (linear numerical simulations)

as Ri_g increases, the slope of isopycnals and hence characteristics of vertically-propagating inertial waves, c.f. (12), is reduced. Consequently, the amplification of the waves by the compression of ray tubes during critical reflection (c.f. Fig. 6) is less intense. Since the waves in the boundary layer are weaker, the energy exchange with the front is reduced. For the strongest fronts (with Richardson numbers near one), however, the rate of energy exchange is comparable to the incoming energy flux of the waves, suggesting that critical reflection of inertial waves at fronts acts as a damping mechanism for the balanced circulation that depends externally on the processes that generate the inertial waves either locally or non-locally, such as the tides or the winds.

5 Near-inertial waves in fronts undergoing frontogenesis

The wave-mean flow interactions that have been described thus far involve fronts with lateral density gradients that do

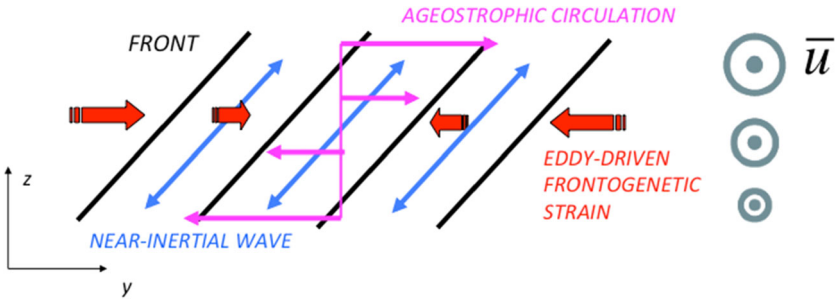

Fig. 9 Flow configuration used in the theory to study NIWs in a front undergoing frontogenesis. A front (with isopycnals in *black*) is forced by a frontogenetic strain field (*red arrows*). Both the density gradient and strain are spatially-uniform and the domain is unbounded. To maintain the thermal-wind balance in the presence of strain, a vertically-sheared ageostrophic secondary circulation (with velocity vectors in *magenta*) is induced. A two-dimensional (i.e., invariant in the x-direction) near-inertial wave (with phase lines shown in *blue*) is added to the flow

not change with time. In the ocean, however, the strength of fronts is rarely stationary, but evolves in response to frontogenetic and frontolytic processes. Strain imposed by the flow of mesoscale eddies is particularly effective at modifying lateral density gradients. When the strain is frontogenetic, it leads to a rapid intensification of the thermal wind shear and a decrease in the gradient Richardson number of the frontal, geostrophic flow (7). As a result, NIWs caught up in a front undergoing frontogenesis, should experience considerable modifications to their dispersion and polarization relations (e.g., Section 2), that could foster wave-mean flow interactions. This idea was explored in the theory of Thomas (2012), which will be summarized here and illustrated with a numerical simulation.

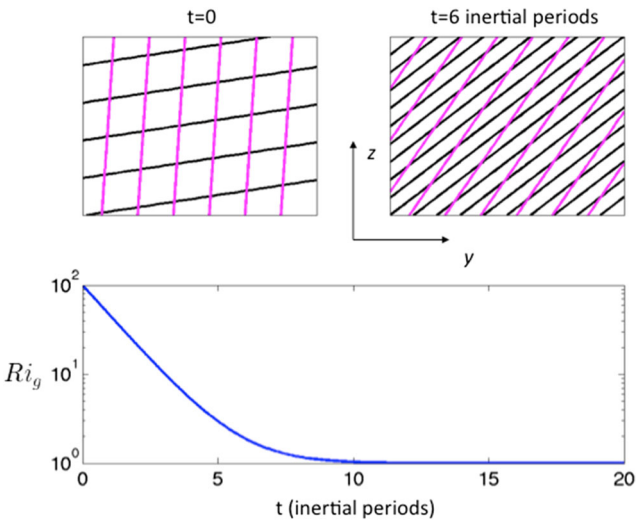

Fig. 10 Surfaces of constant absolute momentum M_g, (*magenta*) and isopycnals (*black*) of the frontal zone schematized in Fig. 9 at the onset of frontogenesis, *top left*, and six inertial periods later, *top right*, for a front forced by a strain of strength $\alpha = 0.0625 f$. The gradient Richardson number of the frontal flow, Ri_g, is plotted as a function of time in the *bottom panel* and in this particular example is initially equal to 100 but asymptotes to one under frontogenesis

As in the front-NIW interactions studies described in the previous sections, Thomas (2012) used the simple "frontal-zone" configuration with spatially-uniform gradients in the density and flow fields (e.g., Fig. 9). In contrast to those studies, the frontal zone is forced by an additional flow $(u_e, v_e) = (\alpha x, -\alpha y)$ with a constant strain, α, that is frontogenetic. This flow is balanced and is meant to represent a mesoscale eddy-driven strain field. The strain throws the front out of the thermal wind balance, and drives an ageostrophic circulation to restore geostrophy. For this simple configuration, the ageostrophic flow is in the cross-front direction, is sheared in the vertical, and drives restratification (Fig. 9, magenta arrows). In spite of the strengthening stratification, however, Ri_g decreases in time because of the exponentially-growing thermal wind shear (Fig. 10, lower panel). The Richardson number of the frontal flow eventually asymptotes to one, reflecting the tendency for frontogenesis to cause surfaces of constant density and absolute momentum to run parallel to one another over time (Fig. 10, top panels).[4]

To this background flow, Thomas (2012) added a two-dimensional near-inertial wave (i.e., invariant in the along-front direction) with streamlines that run parallel to isopycnals (Fig. 9, blue lines) and solved for the evolution of its velocity. In the absence of frontogenetic forcing, this wave would correspond to the inertial-gravity wave of minimum frequency described in Section 2. However, because of the time-dependent nature of the background flow and the presence of ageostrophic shear, the wave is not a simple periodic motion with stationary frequency and amplitude. For early times when Ri_g is large, the amplitude and frequency are relatively constant and the two horizontal components of the velocity oscillate in quadrature as a near-inertial motion (Fig. 11, top panel). However, as the front strengthens

[4]Note that for this simple frontal zone without vertical vorticity, the slope of $M-$surfaces is $s_M = f^2/S^2 = Ri_g s_\rho$. Hence as $Ri_g \to 1$, s_M approaches the isopycnal slope s_ρ.

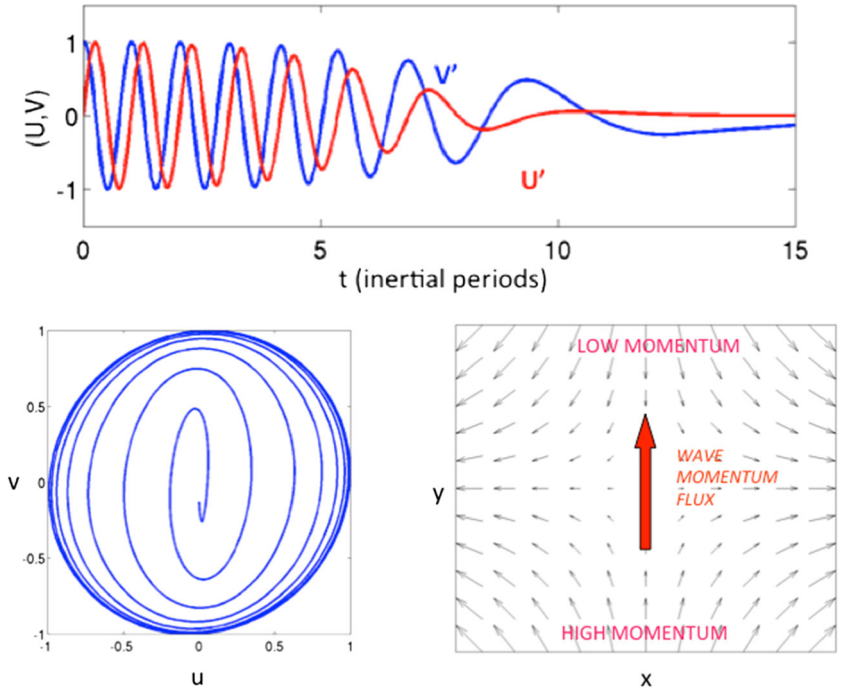

Fig. 11 *Top panel*: Change in the along-front, u' (*red*), and cross-front, v' (*blue*), components of the velocity (both normalized by the initial speed of fluid velocity of the wave) of a near-inertial wave in the background flow undergoing frontogenesis shown in Fig. 10. The time series is made in a frame moving with the background flow, therefore the lengthening of the wave period reflects changes in the intrinsic rather than Eulerian frequency of the wave. *Bottom left panel*: a hodograph of the velocities in the top panel (from $t = 0$ to 15 inertial periods) reveals how a near-inertial wave in a front undergoing frontogenesis experiences a change in polarization relation, transitioning from being circularly polarized to rectilinear in the cross-front, y-direction. In the process, the wave induces a momentum flux that is down the gradient in momentum associated with the eddy-driven strain field whose velocity $(\alpha x, -\alpha y)$ is shown in plan view in the *bottom right*

and Ri_g asymptotes to 1, both the wave's frequency and amplitude decrease. The reduction in amplitude is more pronounced for the along-front versus cross-front component of the velocity (u' and v', respectively), making the velocity hodograph shift from an inertial circle early in the record to a more rectilinear flow in the cross-front direction over time (Fig. 11, lower left panel). This behavior is consistent with the effect that lateral density gradients have on the polarization relation of NIWs described in Section 2, and can be understood in terms of conservation of absolute momentum. As the front strengthens and isopycnals and M-surfaces align, along-isopycnal wave parcel displacements cross fewer and fewer M-surfaces over time, therefore reducing the amplitude of the along-front velocity perturbation u' required to conserve absolute momentum. As u' weakens, so too does the Coriolis force that provides the restoring force for the oscillation, and consequently the periods between velocity minima and maxima expand as frontogenesis progresses (Fig. 11, top panel).

The wave is ultimately damped, however, not by friction as the theory is inviscid, but by transferring kinetic energy to the background flow. The wave can exchange energy with all three elements of the background flow: the thermal wind shear, the balanced eddy strain field, and the cross-front ageostrophic shear at rates $\mathrm{GSP} = -u'w'(S^2/f)$,

$$\mathrm{DSP} = -u'^2\frac{\partial u_e}{\partial x} - v'^2\frac{\partial v_e}{\partial y} = \alpha(v'^2 - u'^2) \tag{17}$$

and AGSP (e.g., Eq. 13, where $\overline{v}$ in this context represents the ageostrophic flow driven by frontogenesis), respectively. These three shear production terms can be non-zero only if the waves induce a vertical flux of momentum, or if their horizontal momentum flux is anisotropic. Fronts allow this to happen by modifying the wave polarization relations, as discussed in Section 2 and as manifest in the solution shown in Fig. 11. Time integrals of the three shear production terms reveal that the waves lose KE to the ageostrophic shear via AGSP (Fig. 12, red line). Surprisingly, however, the waves lose twice the amount of KE that they started with through this mechanism. The additional KE that can account for this discrepancy originates from the strain field via DSP (Fig. 12, black line), which only becomes a major player in the wave energetics when the wave velocity becomes rectilinear and $|v'|$ exceeds $|u'|$ and Eq. 17 becomes positive. The dominance of the cross-front wave velocity at this time drives a momentum flux v'^2 that is down the gradient of v_e

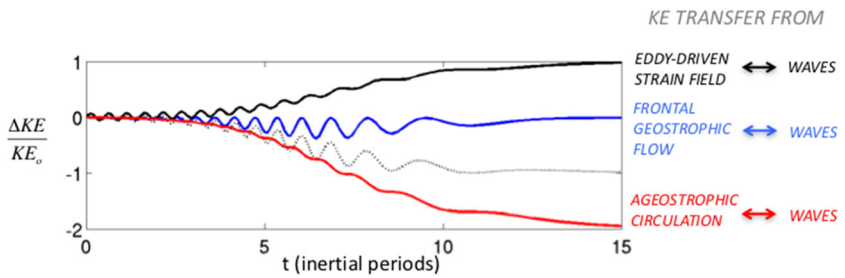

Fig. 12 The transfer of KE to the near-inertial wave shown in Fig. 11 from the eddy-driven strain field, $\int_0^t DSP/KE_o dt'$ (*black*), the frontal geostrophic flow, $\int_0^t GSP/KE_o dt'$ (*blue*), and the ageostrophic circulation, $\int_0^t AGSP/KE_o dt'$ (*red*). The *dotted black line* is the sum of all three terms and represents the net change in KE of the wave. All quantities are normalized by the initial KE of the wave, KE_o

(Fig. 11, lower right panel). In this way, the waves act like a viscosity for the balanced eddy-driven strain field. The KE transferred from the deformation field is ultimately lost to the unbalanced ageostrophic circulation through shear production, hence the waves play a catalytic role in loss of balance. The energy exchange is quite rapid, occurring over a few inertial periods, and scales with the KE initially contained in the waves. Given the large amount of KE in NIWs and the ubiquitous combination of eddy strain and fronts in the ocean, this mechanism could play a significant role in the removal of KE from both the internal wave and mesoscale eddy fields.

In spite of the many simplifying assumptions for the flow configuration used in the theory of Thomas (2012) (e.g., the frontal gradients and strain considered were spatially uniform and the flow was unbounded) the predictions of the theory are qualitatively borne out in numerical experiments of NIWs in strained fronts with more realistic flow fields. One such numerical experiment will be presented here, while a more thorough examination is described in Thomas (2017). The numerical simulation is configured with a front that is aligned in the x-direction, with initially uniform gradients, and in a periodic channel with walls on the northern and southern boundaries of the domain (Fig. 13, left panel). The front is in geostrophic balance, and an array of barotropic eddies is added to the flow to generate strain. The strain is frontogenetic near $y = 37.5$ km, $x = 18.75$ km and frontolytic near $y = 37.5$ km, $x = 56.25$ km (Fig. 13). To this flow, a NIW is added that takes the form of a beam (Fig. 14, upper panels). The beam is not forced but is instead constructed as an initial condition with a plane wave of frequency $1.025f$ modulated by a Gaussian envelope with an e-folding scale of 30 m in the vertical and 5.6 km in the horizontal. The response of the wave to frontogenetic versus frontolytic strain is markedly different (c.f. Figs. 14 and 15 left and right panels). In regions of frontolysis, the horizontal wavenumber of the wave decreases as isopycnals flatten and the front weakens. The wave essentially retains its inertial character throughout the simulation as reflected in its velocity hodograph that traces inertial circles (Fig. 15 right panel). In contrast, in regions of frontogenesis the properties of the wave change dramatically: the horizontal wavenumber increases, the amplitude decreases, and the velocity becomes more rectilinear in the cross-front direction with

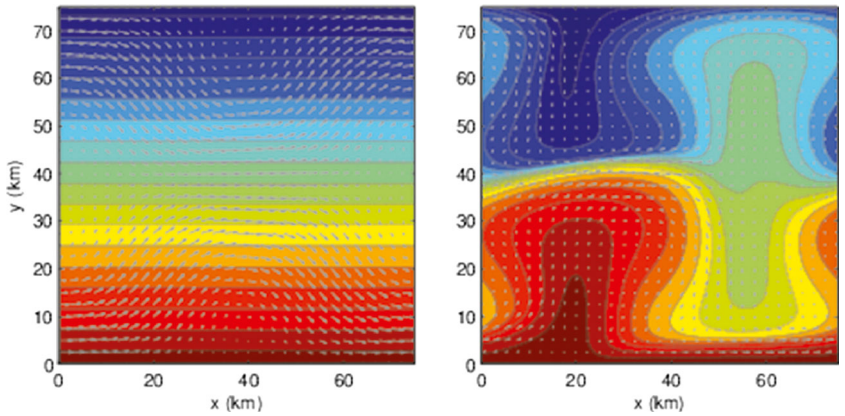

Fig. 13 Plan view of the surface buoyancy and velocity fields at $t = 0$ (*left*) and 7.1 inertial periods (*right*) from the numerical simulation used to study NIWs in a front undergoing frontogenesis. The eddy field that drives frontogenesis (frontolysis) near $x = 18.75$ km, $y = 37.75$ km ($x = 56.25$ km, $y = 37.75$ km) has an initial maximum strain rate of $0.045f$. The color scale is the same in both panels and spans buoyancy values between -3.55×10^{-3} and 3.55×10^{-3} m s^{-2}

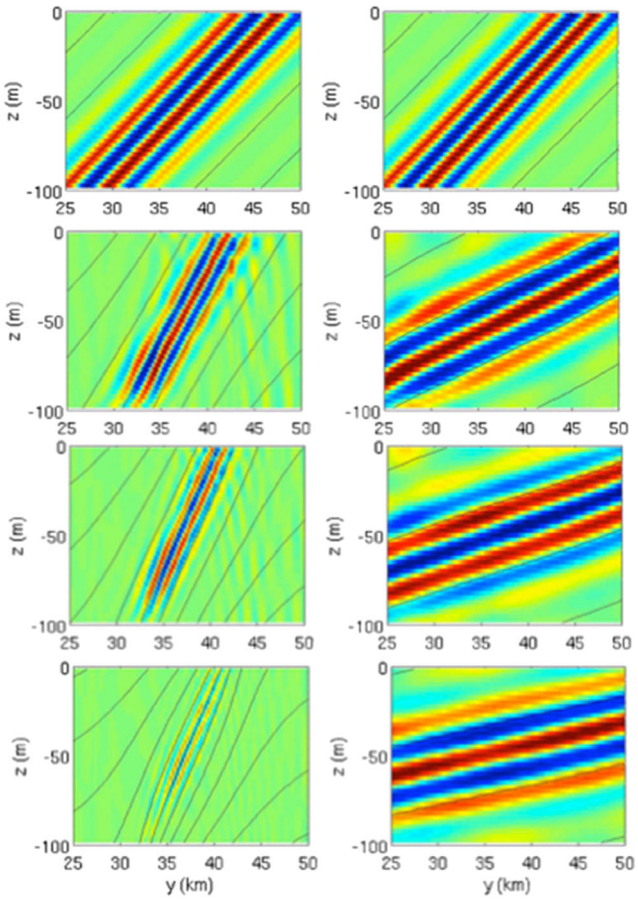

Fig. 14 Cross-sections of the y-component of the wave velocity field (color) and isopycnals (contours) at, from *top* to *bottom*, $t = 0$, 2.9, 4.3, and 5.7 inertial periods into the numerical simulation used to study NIWs in a front undergoing frontogenesis. The sections on the *left* (*right*) were made at $x = 18.75$ km ($x = 56.25$ km) in a region where the eddy-driven strain field is frontogenetic (frontolytic). The color scale is the same in each panel and spans velocities between -0.01 and 0.01 m s^{-1}. The contour interval for the density is 0.08 kg m^{-3} in each panel

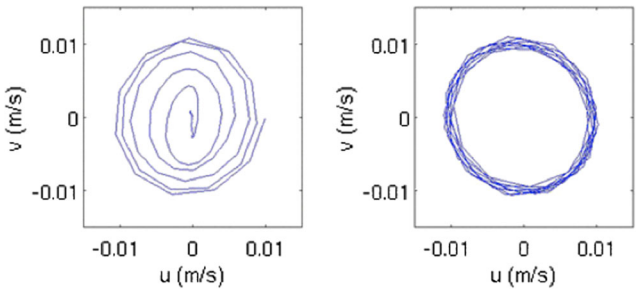

Fig. 15 Hodographs of the wave velocity at mid-depth ($z = -50$ m), $y = 37.5$ km, and traced between 0 and 8 inertial periods from the numerical simulation used to study NIWs in a front undergoing frontogenesis. The hodograph on the *left* (*right*) was made at $x = 18.75$ km ($x = 56.25$ km) in a region where the eddy-driven strain field is frontogenetic (frontolytic)

time (Figs. 14 and 15 left panels). The modifications to the NIW in the front undergoing frontogenesis is therefore qualitatively consistent with the theory (e.g., Fig. 11).

A more quantitative comparison to the theory can be made by calculating the transfers of KE between the NIW and background flow. The strongest energy exchanges are confined to the region of frontogenesis. In this region, by eight inertial periods into the experiment, the waves have removed an amount of KE from the strain field, $\int DSPdt'$, that is comparable to the initial KE in the NIW (c.f. Fig. 16 left and right panels). At the same time, the NIWs lose a significant amount of KE to the ageostrophic circulation, i.e. $\int AGSPdt' < 0$, but exchange little energy with the frontal geostrophic flow, $\int GSPdt'$, averaged over the frontal zone (e.g., Fig. 17). Other simulations with a plane wave that is not modulated in the horizontal by a Gaussian envelope shows similar behavior, indicating that the enhancement and confinement of the energy exchange at the front is a result of the frontal dynamics, not the initial position and lateral extent of the wave (Thomas 2017). The behavior is consistent with the theory (e.g., Fig. 12, black line), but unlike the theory, the energy exchange occurs in a narrow area delineated by the finite width of the front.

The NIW in the simulation described above had an initial horizontal wavelength, λ_y that was smaller than the width of the front, L_f. The opposite limit, $\lambda_y > L_f$, is considered more representative of the ocean since the lateral wavelength of NIWs is thought to be imposed by the winds which typically vary on larger scales than oceanic flows. To explore the impact of frontogenesis on NIWs with $\lambda_y > L_f$ another experiment was performed with an initial wave field with no horizontal wavenumber, but with the same front and eddy field shown in Fig. 13. Cross-sections of the wave velocity for this experiment reveal that in the region of frontogenesis the wave develops a horizontal wavenumber in a matter of a few inertial periods (Fig. 18). The horizontal variability in the wave field is generated by the frontal vertical circulation which is characterized by downwelling and upwelling on the dense and light sides of the front, respectively. This differential vertical motion tilts wave phase lines in the opposite direction of isopycnals in the center of the front, which allows the NIWs to radiate away from the front, explaining the deficit in wave energy seen there at 9 inertial periods. On the flanks of the front, however, the NIWs are trapped as the differential vertical motion aligns the wave phase lines with isopycnals, thus reducing the group velocity, e.g., (11). This numerical experiment illustrates that frontogenesis can significantly affect NIWs even when they initially have no lateral variations and in particular can facilitate the radiation of NIW energy from the surface to the ocean interior.

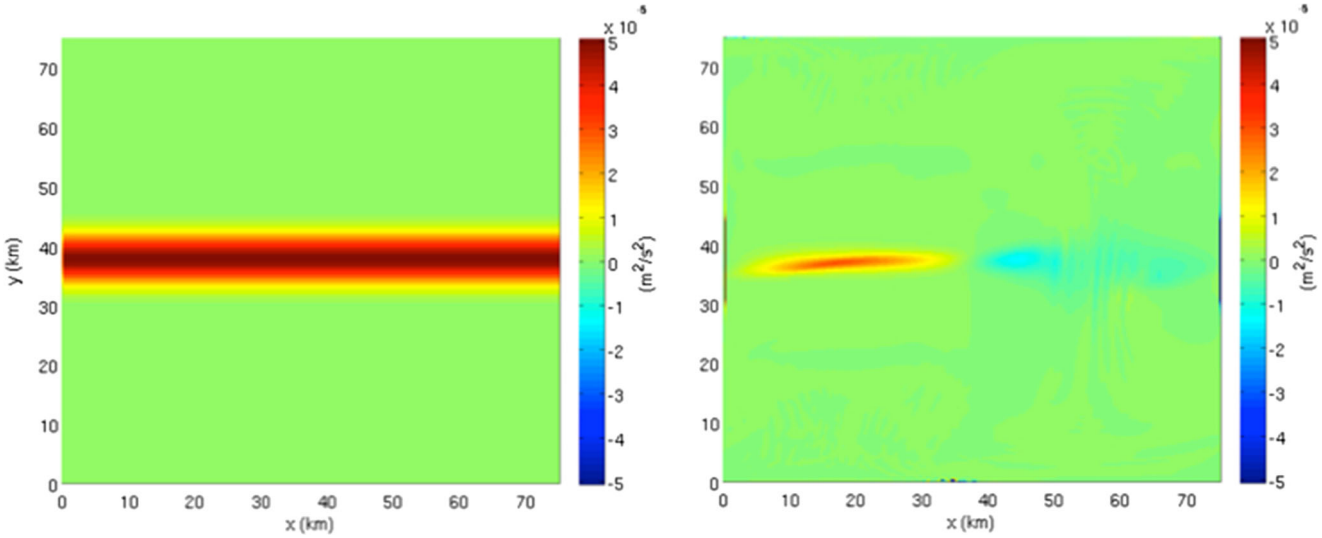

Fig. 16 *Left*: plan view of the KE in the NIW at the start of the numerical simulation used to study NIWs in a front undergoing frontogenesis. *Right*: plan view of the amount of KE removed from the strain field by the NIWs, i.e., $\int DSPdt$, eight inertial periods into the simulation. The color scale is the same in both panels and both quantities are evaluated at mid-depth ($z = -50$ m)

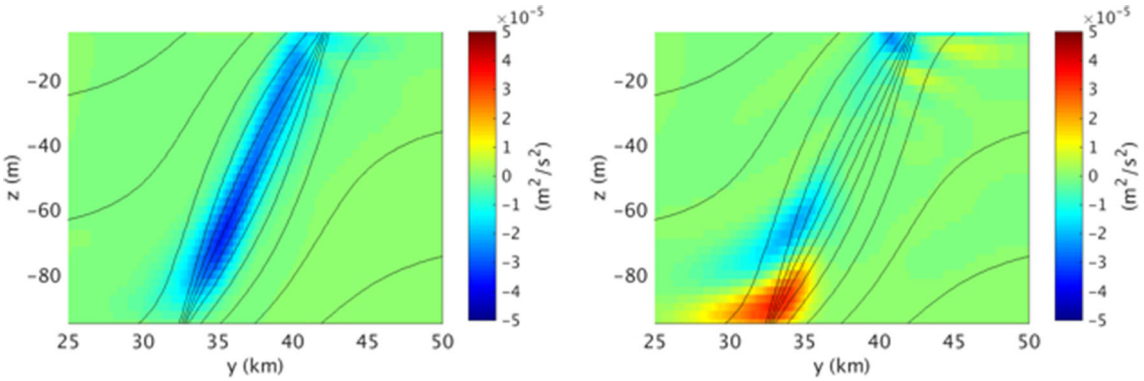

Fig. 17 *Left*: cross-section of the amount of KE removed from the ageostrophic flow by the NIWs, i.e., $\int AGSPdt$, eight inertial periods into the simulation used to study NIWs in a front undergoing frontogenesis. *Right*: cross-section of the amount of KE removed from the frontal geostrophic flow by the NIWs, i.e., $\int GSPdt$, eight inertial periods into the simulation. The color scale in both panels is the same as in Fig. 16 and both quantities are evaluated at $x = 18.75$ km in a region where the eddy-driven strain field is frontogenetic. Isopycnals are contoured with an interval of 0.08 kg m^{-3} in both panels

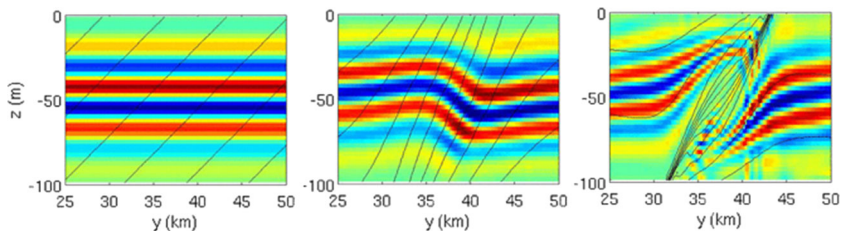

Fig. 18 Cross-sections of the y-component of the wave velocity field (color) and isopycnals (contours) at, from left to right, $t = 0, 5$, and 9 inertial periods into a numerical simulation of a NIW with initially no horizontal wavenumber in a front undergoing frontogenesis. The sections were made at $x = 18.75$ km in a region where the eddy-driven strain field is frontogenetic. The color scale is the same in each panel and spans velocities between -0.01 and 0.01 m s^{-1}. The contour interval for the density is 0.08 kg m^{-3} in each panel

6 Conclusions

Winds are one of the main sources of KE for the ocean and generate NIWs and balanced currents. How the KE contained in these motions is transferred to small scales and dissipated is not well understood. Wave-mean flow interactions have been invoked as a mechanism that could facilitate this process. Here, it is shown that ocean fronts, which are a ubiquitous feature of the upper-ocean, provide conditions conducive for irreversible energy exchanges between NIWs, balanced motions, and small-scale turbulence by modifying the properties of the waves in rather surprising ways.

In fronts, inertia-gravity waves are permitted to have subinertial frequencies, more accurately, frequencies that are less than the effective inertial frequency $f_{eff} = f\sqrt{1+Ro_g}$. Consequently, at fronts, NIWs can be susceptible to a parametric subharmonic instability that transfers KE from the waves to subinertial motions with smaller vertical scales; subsequent development of secondary instabilities irreversibly convert the NIW KE to potential energy and heat through mixing and viscous dissipation. This PSI develops in stratified frontal flows with Richardson numbers just above one, well above the condition for Kelvin-Helmholtz instability. Such conditions are likely to be found at the base of the surface mixed layer in the ocean. It is precisely in this region where inertial shears, the source of energy for the PSI, are observed to be strongest and where much of the near-surface dissipation of inertial motions is thought to occur (Plueddemann and Farrar 2006). Could PSI facilitate this dissipation? To investigate this possibility more fully, the effects on the instability of vertically-varying stratification and shear should be studied.

The four directions that energy in an inertia-gravity wave can propagate are symmetric about the isopycnal slope, not the horizontal, which at a front can profoundly alter the rules of wave reflection off surfaces. In particular, inertial waves with frequency f_{eff} experience critical reflection off the sea surface at fronts. Upon reflection, the vertical scale of the waves collapses, enhancing viscous dissipation. But in the process, the waves dissipate more energy than that which they flux toward the surface. The extra energy comes from the front. Thus, critical reflection at fronts is a mechanism that dissipates energy in the NIW field and the balanced circulation simultaneously. It is therefore distinct from classical critical reflection of internal waves off bathymetry which only damps the waves. The rate at which energy is removed and dissipated from the front during critical reflection scales with the energy flux of the upward propagating inertial waves. Accounting for variations in the effective Coriolis frequency, such waves could be generated remotely by the winds or tides, for example, and experience critical reflection if their frequency is equal to the local value of f_{eff} at the front. In this case, the dissipation of energy in the balanced circulation via critical reflection should scale with the rate of energy input into the waves by the winds or tides where they are generated. Another complication to consider is variable stratification near the surface of the ocean. For example, if there were a mixed layer, the theory would predict that the energy exchange with the mean flow during critical reflection would be enhanced as the weaker stratification reduces the Richardson number of the geostrophic flow (e.g., Fig. 8).

Finally, the velocity hodographs of NIWs do not trace horizontal inertial circles at fronts. Instead, the wave velocity has a vertical component and is elliptically polarized with stronger flow in the cross-front direction. These modified polarization relations allow the waves to exchange kinetic energy with mean flows by driving wave momentum fluxes. The effects are enhanced with frontal intensity, and therefore are most pronounced in fronts undergoing frontogenesis. If the frontogenesis is driven by strain associated with mesoscale eddies, for example, the increasingly elliptically polarized wave velocities allow NIWs trapped in a front to efficiently extract KE from eddies. The energy is not stored in the wave field but is instead lost to cross-front ageostrophic motions. Hence, the NIWs act as a conduit that transfers KE from balanced eddies to unbalanced motions. As with critical reflection, the waves are ultimately damped in the process, therefore both mechanisms represent sinks of KE for the NIW wave field and mesoscale eddies.

Recent numerical studies on energy exchanges between low-frequency currents and NIWs suggest that the baroclinicity of the balanced flow is critical for such exchanges. Taylor and Straub (2016) and Barkan et al. (2017) diagnosed terms in low and high pass filtered energy equations from simulations of wind-forced channel flows to quantify the energy transfer between the higher frequency NIWs and low frequency motions. Both studies found that the NIWs damped the low-frequency motions and that shear production terms involving the vertical shear of the low frequency flow played a leading order role in the energetics. Such terms are absent in NIW-mean flow interactions in barotropic balanced flows (e.g., as described by Xie and Vanneste 2015 and Wagner and Young 2016) and point to the importance of fronts in facilitating energy transfers across scales and frequencies. Whether the mechanisms described in this review were active in the simulations of Taylor and Straub (2016) and Barkan et al. (2017) is difficult to assess without a detailed analysis, but nonetheless both articles motivate further study of the role of baroclinic currents in NIW-mean flow interactions.

The rate and amount of KE removed from balanced motions by the processes described here could be significant for global energy budgets since the theory suggests that they should scale with the NIW-generating energy fluxes and the KE contained in NIWs, respectively. For example, NIWs

in a front undergoing frontogenesis remove an amount of KE from the strain field that is about equal to the KE that they contain. This energy removal happens in a short period of time, namely in a few inertial periods $\sim 1 \times 10^5$ s, since frontogenesis and its modification to NIWs is an exponentially-fast process. Globally, it is estimated there is 1×10^{18} J in NIWs (Ferrari and Wunsch 2010). Even if, for example, only 1% of this energy coincided with fronts undergoing frontogenesis, the theory would suggest that NIWs could damp the balanced circulation at a rate of order 0.1 TW, which is around a tenth of the wind-work on the circulation. This begs the question, over which regions of the ocean are NIW-front interactions most prevalent? Clearly, western boundary currents and the Antarctic Circumpolar Current are prime locations since they are where fronts are most intense, meso- and gyre-scale strain is strong, and where the wind energy input to NIWs is maximum (Alford 2003). Indeed, NIWs observed in these regions show indications of being modified by fronts and baroclinic eddies (e.g., Kunze 1986; Rainville and Pinkel 2004; Shcherbina et al. 2003; Joyce et al. 2013; Whitt and Thomas 2013; Nagai et al. 2015; Whitt et al. 2017) and of causing enhanced dissipation (e.g., Kunze et al. 1995; Inoue et al. 2010). Observations of NIWs in less intense fronts, such as those in the subtropical convergence zones, also suggest that interactions of NIWs with baroclinic mean flows can be significant (e.g., Kunze and Sanford 1984; Alford et al. 2013), implying that the phenomenon may be ubiquitous and therefore play an important role in closing the kinetic energy budget of the ocean. Yet many details of NIW-front interactions, from regional variations to the effects of finite-width fronts, need to be understood before the contributions of these processes to global energy budgets can be fully quantified, and studies addressing these issues should be the focus of future work.

Acknowledgements This article reviews material that I was invited to present at the 48th Liege Colloquium on Submesoscale Processes: Mechanisms, Implications and New Frontiers. I would like to thank Alexander Barth, Eric Deleesnijder, Amala Mahadevan, Ananda Pascual, Simon Ruiz, and Charles Troupin for organizing such a stimulating meeting and inviting me to speak. This work was funded by the National Science Foundation grant OCE-1260312.

References

Alford M (2003) Redistribution of energy available for ocean mixing by long-range propagation of internal waves. Nature 423:159–163

Alford M, Gregg M (2001) Near-inertial mixing: modulation of shear,strain and microstructure at low latitude. J Geophys Res 106:16,947–16,968

Alford M, Shcherbina AY, Gregg MC (2013) Observations of near-inertial internal gravity waves radiating from a frontal jet. J Phys Oceanogr 43:1225–1239

Balmforth NJ, Young WR (1999) Radiative damping of near-inertial oscillations in the mixed layer. J Mar Res 57:561–584

Barkan R, Winters KB, McWilliams JC (2017) Stimulated imbalance and the enhancement of eddy kinetic energy dissipation by internal waves. J Phys Oceanogr 47:181–198

Eliassen A (1962) On the vertical circulation in frontal zones. Geofys Publ 24:147–160

Elipot S, Lumpkin R, Prieto G (2010) Modification of inertial oscillations by the mesoscale eddy field. J Geophys Res 115:C09,010

Ferrari R, Wunsch C (2009) Ocean circulation kinetic energy: reservoirs, sources, and sinks. Annu Rev Fluid Mech 41:253–282

Ferrari R, Wunsch C (2010) The distribution of eddy kinetic and potential energies in the global ocean. Tellus A 62:92–108

Grisouard N, Thomas LN (2015) Critical and near-critical reflections of near-inertial waves off the sea surface at ocean fronts. J Fluid Mech 765:273–302

Grisouard N, Thomas LN (2016) Energy exchanges between density fronts and near-inertial waves reflecting off the ocean surface. J Phys Oceanogr 46:501–516

Healey D, LeBlond PH (1969) Internal wave propagation normal to a geostrophic current. J Mar Res 27:85–98

Holton JR (2004) An introduction to dynamic meteorology, 4th edn. International Geophysics Series, Elsevier Academic Press, Burlington, MA

Inoue R, Gregg MC, Harcourt RR (2010) Mixing rates across the Gulf Stream, part 1: on the formation of eighteen degree water. J Mar Res 68:643–671

Ivey GN, Nokes RL (1989) Vertical mixing due to the breaking of critical internal waves on sloping boundaries. J Fluid Mech 204:479–500

Joyce T, Toole J, Klein P, Thomas L (2013) A near-inertial mode observed within a Gulf Stream warm core ring. J Geophys Res 118:1–10. doi:10.1002/jgrc.20141

Kunze E (1985) Near-inertial wave propagation in geostrophic shear. J Phys Oceanogr 15:544–565

Kunze E (1986) The mean and near-inertial velocity fields in a warm-core ring. J Phys Oceanogr 16:1444–1461

Kunze E, Boss E (1998) A model for vortex-trapped internal waves. J Phys Oceanogr 28:2104–2115

Kunze E, Sanford T (1984) Observations of near-inertial waves in a front. J Phys Oceanogr 14:566–581

Kunze E, Schmidt RW, Toole JM (1995) The energy balance in a warm-core ring's near-inertial critical layer. J Phys Oceanogr 25:942–957

McComas CH, Bretherton FP (1977) Resonant interaction of oceanic internal waves. J Geophys Res 82:1397–1412

Mooers CNK (1975) Several effects of a baroclinic current on the cross-stream propagation of inertial-internal waves. Geophys Fluid Dyn 6:245–275

Müller P, Holloway G, Henyey F, Pomphrey N (1986) Nonlinear interactions among internal gravity waves. Rev Geophys 24:493–536

Nagai T, Tandon A, Kunze E, Mahadevan A (2015) Spontaneous generation of near-inertial waves by the Kuroshio front. J Phys Oceanogr 45:2381–2406

Olbers DJ (1981) The propagation of internal waves in a geostrophic current. J Phys Oceanogr 11:1224–1233

Plueddemann AJ, Farrar JT (2006) Observations and models of the energy flux from the wind to mixed-layer inertial currents. Deep-Sea Res II 53:5–30

Polzin KL (2010) Mesoscale eddy-internal wave coupling. Part II: energetics and results from PolyMode. J Phys Oceanogr 40:789–801

Polzin KL, Lvov YV (2011) Toward regional characterizations of the oceanic internal wavefield. Rev Geophys 49:rG4003. doi:10.1029/2010RG000329

Rainville L, Pinkel R (2004) Observations of energetic high-wavenumber internal waves in the Kuroshio. J Phys Oceanogr 34:1495–1505

Sawyer JS (1956) The vertical circulation at meterological fronts and its relation to frontogenesis. Proc R Soc Lond A 234:346–362

Shakespeare C, Taylor J (2014) The spontaneous generation of inertia–gravity waves during frontogenesis forced by large strain: theory. J Fluid Mech 757:817–853

Shakespeare CJ, Hogg A (2017) Spontaneous surface generation and interior amplification of internal waves in a regional-scale ocean model. J Phys Oceanogr 47:811–826

Shakespeare CJ, Taylor JR (2013) A generalized mathematical model of geostrophic adjustment and frontogenesis: uniform potential vorticity. J Fluid Mech 736:366–413. doi:10.1017/jfm.2013.526

Shcherbina AY, Talley LD, Firing E, Hacker P (2003) Near-surface frontal zone trapping and deep upward propagation of internal wave energy in the Japan East Sea. J Phys Oceanogr 33:900–912

Taylor S, Straub D (2016) Forced near-inertial motion and dissipation of low-frequency kinetic energy in a wind-driven channel flow. J Phys Oceanogr 46:79–93

Thomas LN (2012) On the effects of frontogenetic strain on symmetric instability and inertia-gravity waves. J Fluid Mech 620–640

Thomas LN (2017) Near-inertial waves in fronts undergoing frontogenesis. J Phys Oceanogr in preparation

Thomas LN, Taylor JR (2014) Damping of inertial motions by parametric subharmonic instability in baroclinic currents. J Fluid Mech 743:280–294

van Meurs P (1998) Interactions between near-inertial mixed layer currents and the mesoscale: the importance of spatial variabilities in the vorticity field. J Phys Oceanogr 28:1363–1388

Vanneste J (2013) Balance and spontaneous wave generation in geophysical flows. Ann Rev Fluid Mech 45:147–172

Wagner G, Young W (2016) A three-component model for the coupled evolution of near-inertial waves, quasi-geostrophic flow and the near-inertial second harmonic. J Fluid Mech 802:806–837

Whitt DB, Thomas LN (2013) Near-inertial waves in strongly baroclinic currents. J Phys Oceanogr 43:706–725

Whitt DB, Thomas LN, Klymak JM, Lee CM, D'Asaro EA (2017) Trapped super-inertial waves in the Gulf Stream. J Phys Oceanogr Submitted

Xie JH, Vanneste J (2015) A generalised-Lagrangian-mean model of the interactions between near-inertial waves and mean flow. J Fluid Mech 774:143–169

Young WR, Ben-Jelloul M (1997) Propagation of near-inertial oscillations through a geostrophic flow. J Mar Res 55:735–766

Zeitlin V, Reznik GM, Ben Jelloul M (2003) Nonlinear theory of geostrophic adjustment. Part 2. Two layer and continuously stratified primitive equations. J Fluid Mech 491:207–228